# From Impurity Doping to Metallic Growth in Diffusion Doping: Properties and Structure of Silver-Doped InAs Nanocrystals

Yorai Amit,[†,‡] Yuanyuan Li,[§] Anatoly I. Frenkel,[*,§] and Uri Banin[*,†,‡]

[†]The Institute of Chemistry and [‡]The Center for Nanoscience and Nanotechnology, Hebrew University, Jerusalem 91904, Israel and [§]Department of Physics, Yeshiva University, New York, New York 10016, United States

ABSTRACT Tuning of the electronic properties of presynthesized colloidal semiconductor nanocrystals (NCs) by doping plays a key role in the prospect of implementing them in printed electronics devices such as transistors and photodetectors. While such impurity doping reactions have already been introduced, the understanding of the doping process, the nature of interaction between the impurity and host atoms, and the conditions affecting the solubility limit of impurities in nanocrystals are still unclear. Here, we used a postsynthesis diffusion-based doping reaction to introduce Ag impurities into InAs NCs. Optical absorption spectroscopy and analytical inductively coupled plasma mass spectroscopy (ICP-MS) were used to present a two-stage doping model consisting of a "doping region" and a "growth region", depending on the impurity to NC ratio in the

reaction vessel. X-ray absorption fine-structure (XAFS) spectroscopy was employed to determine the impurity location and correlate between the structural and electronic properties for different sizes of InAs NCs and dopant concentrations. The resulting structural model describes a heterogeneous system where the impurities initially dope the NC, by substituting for In atoms near the surface of the NC, until the "solubility limit" is reached, after which the rapid growth and formation of metallic structures are identified.
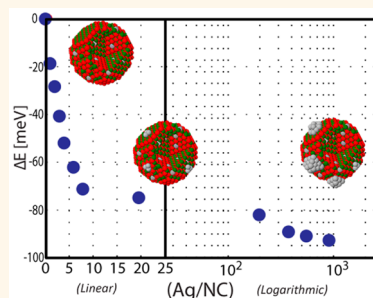
KEYWORDS: colloidal nanocrystals · impurity doping · solubility limit · XAFS · EXAFS · XANES

Colloidal semiconductor nanocrystals (NCs) manifest unique size-dependent optoelectronic properties.[1,2] Advancements in the synthesis of semiconductor NCs enable the use of different semiconductor materials[3–5] and the fabrication of highly controlled shapes[6–8] and various compositions[9–11] as means of further controlling their electronic properties. The ability to tune the electronic properties of semiconductor NCs has led to the demonstrations of various applications based on NC building blocks.[12–14] The process of doping, which is well known for bulk semiconductors, presents an additional method for controlling the physical properties of semiconductor materials and as a result led to the demonstration of numerous optoelectronic applications.[15] Therefore, great efforts have been put into the prospect of doping semiconductor colloidal nanocrystals.[16–20] To this end, the doping of semiconductor NCs has been demonstrated via

in situ methods, by adding impurities to the reaction vessel[21–26] or ex situ such as electrochemical reactions,[27,28] thermal treatments,[29,30] and the more conventional impurity doping process, where the impurities are introduced into the semiconductor lattice postsynthesis.[31–33] However, impurity doping of nanocrystals is still considered a difficult task, mainly due to "self-purification" processes, owing to the small size of the NC, resulting in the expulsion of the impurities to the surface of the NC.[34–36] This was previously described for InAs NCs, where the root-mean-square distance that a diffusing atom would travel in 24 h was found to greatly exceed the size of the NCs.[31] This difficulty was also shown for P doping of Si NCs.[37] Here, a theoretical study revealed a critical size of the NC host, below which the P atoms are expelled to the surface of the NCs.

We have previously presented the synthesis of heavily doped InAs colloidal NCs by

means of a room-temperature, solution-phase, diffusion-based reaction, in which Ag and Cu impurities were introduced to a solution of presynthesized NCs.[31] Scanning-tunneling-spectroscopy (STS) measurements of Cu (Ag)-doped NCs revealed a blue (red) shift of the Fermi energy, proving the n-type (p-type) doping. It was also shown that neither the crystal structure nor the size of the NCs was affected by the doping reaction, ruling out the possibility of size-dependent effects governing the observed changes in the optoelectronic properties. In a following work, we have reported on the detailed characterization of Cu doping of InAs NCs, using advanced X-ray absorption fine structure (XAFS) spectroscopy to establish the location of the impurity and its electronic state within the NC as a function of the impurity to NC ratio in the reaction solution.[38] We found that the diffusion of Cu impurities into the NC lattice is favored and results in an energetically stable system. Furthermore, we identified the impurity site, determining that the Cu impurities occupy only hexagonal-interstitial sites throughout the lattice for a very wide range of impurity concentrations. This is fully consistent with the n-type behavior measured for the Cu-doped InAs both using STM and in optical measurements.[31]

Recently, Norris et al. reported on the Ag doping of CdSe NCs, using also a postsynthesis solution-phase diffusion doping reaction.[32] In their work they have found that the electronic properties of the doped CdSe NCs shift from an n-type to a p-type behavior, as a result of the impurity assuming initially an interstitial site followed by its transformation into a substitutional lattice site, depending on the impurity concentration in the lattice. Subsequent modeling of the system helped to better understand the doping mechanism and the suggested structural transformations. The modeling results indicate that the Ag impurities are initially able to penetrate the lattice by diffusion through interstitial sites, followed by their repulsion to the surface of the NC, where they assume substitutional sites, through the kick-out of the Cd host atoms, and eventually form impurity pairs in both substitutional and interstitial lattice sites.[39]

While Ag exhibits a bimodal behavior in CdSe, the optoelectronic studies of Ag doping in InAs suggest a purely p-type behavior.[31] Further structural analysis is needed in order to fully understand the doping mechanism and the nature of interactions between the impurity and the host in such a system. In our previous work on Cu-doped InAs NCs we addressed some of the intriguing questions dealing with impurity doping in colloidal NCs. First, we have shown that the Cu impurity atoms saturate the lattice by occupying nearly all possible interstitial sites, keeping the host lattice intact, regardless of the Cu concentration. In light of this, it is interesting to realize how the use of a substitutional impurity, such as Ag, would affect the InAs NC lattice.

A second aspect is that of the solubility limit. Cu impurities exhibited no solubility limit in InAs, up to the point of nearly saturating the NC lattice. Ag impurity studied here is much larger than Cu, may have different valence, and thus may reveal a different behavior in terms of its solubility. Furthermore, in NCs, the solubility limit is of great interest due to the possible size effects.

In the current work we present a size-dependent study of Ag-doped InAs NCs using both analytical and spectroscopic methods to better understand the doping mechanism and correlate between the observed changes in the optoelectronic properties and the local environment around the impurity atom for different impurity concentrations. Furthermore, using analytical inductively coupled plasma mass-spectrometry (ICP-MS) measurements together with optical absorption measurements, we were able to identify two regions, a "doping region" and a "growth region", that depend strongly on the concentration of impurities in the reaction solution and point toward an identification of a "solubility limit" of Ag impurities in InAs NCs.

RESULTS AND DISCUSSION

Identification of the Impurity "Solubility Limit". Colloidal InAs NCs were synthesized following a well-established synthesis[40] followed by a size-selective precipitation to obtain narrow size distributions. The presynthesized InAs NCs were then doped with various amounts of Ag impurities by adding calculated volume fractions of the impurity solution containing the metal salt ($AgNO_3$), didodecyldimethylammonium bromide (DDAB, to stabilize the metal salt in the organic solution), and dodecylamine (DDA, which stabilizes the NCs and acts as a reducing agent). Figure S1 of the Supporting Information (SI) presents a set of doping solutions, using the different ligands to stabilize the metal salt, (a) at the time of preparation and (b) after 16 h. TEM image of the resulting product of the $AgNO_3$ in DDA solution after 16 h (Figure S2a) and the XRD diffractogram (Figure S2b) indicate the formation of metallic Ag nanoparticles at room temperature, clearly reflecting the role DDA plays in silver reduction. With DDAB, Ag nanoparticles are not formed, indicating its role in stabilizing Ag(I) in solution. For additional information see the Experimental Methods.

TEM images of the as-synthesized InAs NCs (Figure 1a), which are 4.8 nm in diameter, and the doped InAs NCs (Figure 1b) show that neither the size nor the shape of the NCs is changed upon doping, consistent with our earlier study;[31] see SI Figure S3 for size histograms and additional TEM images of 4.8 nm NCs before and after doping. Figure 1c presents the normalized optical absorption spectra for the 4.8 nm InAs NCs upon addition of various ratios of Ag impurities per NC. The data are shown as a function of the molar ratio of Ag to NCs in solution, in the initial stage, denoted
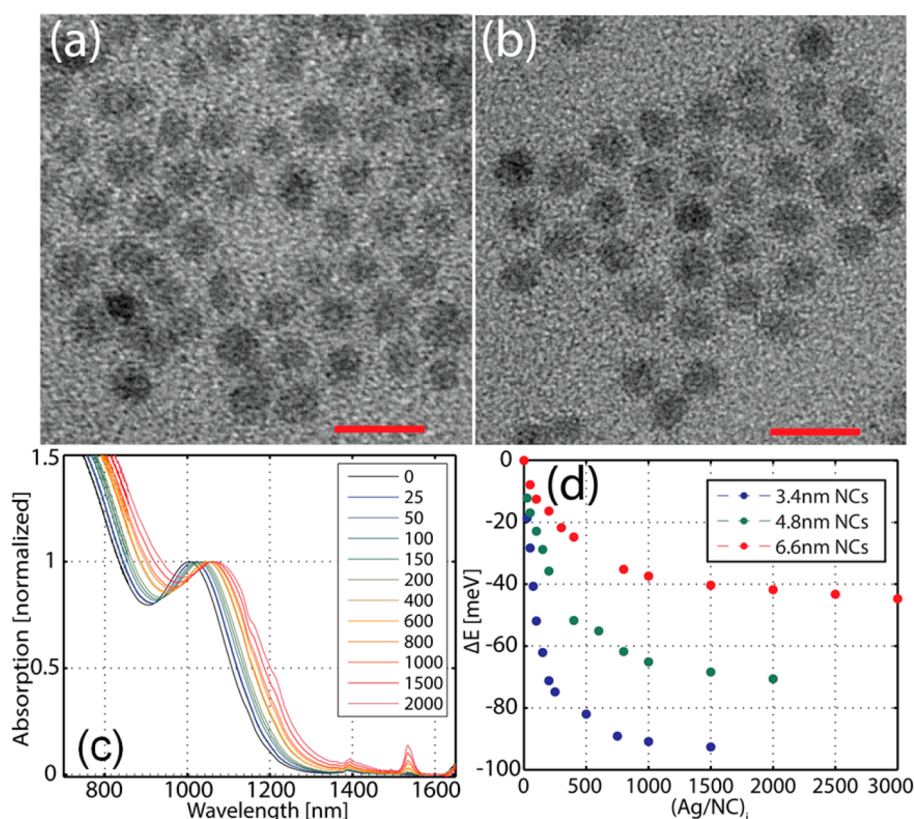
Figure 1. TEM images of 4.8 nm (diameter) InAs NCs (a) before and (b) after doping to a ratio of 400 (Ag/NC)$_i$ in solution (scale bar = 10 nm). (c) Normalized absorption spectra for the 4.8 nm NCs for various ratios of up to 2000 (Ag/NC)$_i$, which denote the ratios of Ag to NC in solution phase. (d) Energy shift of the first exciton peak for 3.4 nm (blue), 4.8 nm (green), and 6.6 nm (red) InAs NCs reacted with increasing amounts of Ag in the solution phase. (For the absorption spectra of the 3.4 and 6.6 nm InAs NCs for the different doping concentrations, see SI Figure S4).

as (Ag/NC)$_i$. As can be seen, the position of the first exciton peak gradually red-shifts[41] when increasing the (Ag/NC)$_i$ ratio in the solution. Previous study using STM, optical spectroscopy, and theoretical analysis showed that the doping leads to a p-type behavior. Specifically, the red-shifted absorption has been interpreted as evidence of band tailing effects related to the disorder induced by impurity insertion into the InAs NC lattice. For additional information and theoretical modeling of the observed spectral shifts see ref 31.

Figure 1d depicts the shift in the position of the first exciton peak, with respect to the undoped samples, for the 3.4 nm (blue), 4.8 nm (green), and 6.6 nm (red) InAs NCs upon reacting them with various (Ag/NC)$_i$ ratios (for the optical absorption spectra of the 3.4 and 6.6 nm doped NCs see SI Figure S4). While all three samples exhibit a red-shift in the electronic structure, differences are noticeable. First, the smaller NCs are more strongly affected by the doping process, completely losing the feature of the first exciton peak when reaching high (Ag/NC)$_i$ ratios (Figure S4a). The larger NCs, however, do not exhibit the same loss of feature, even when exposed to higher (Ag/NC)$_i$ ratios, although some broadening and loss of structure are observed. It is noted that for the larger 6.6 nm NCs (Figure S4b) the apparent loss of feature of the first exciton peak is

induced by ligand absorption at 1200 nm (see SI Figure S5), which intensifies as the doping level is pushed to higher ratios, due to the contribution of the ligands in the impurity solution. The second difference is observed when comparing the extent of the red-shift of the first exciton peak between the three different sizes (Figure 1d). As the NC grows in size, the electronic shift for a given (Ag/NC)$_i$ ratio is reduced, as well as the overall obtainable shift. For instance, whereas the first exciton peak of the 3.4 nm NCs shifts by −70 meV for a ratio of 200 (Ag/NC)$_i$, it reaches values of only −35 and −16 meV for the 4.8 and 6.6 nm NCs, respectively.

Doping experiments were performed over a wide range of molar concentrations, and the measured excitonic shifts were found to, essentially, depend only on the (Ag/NC)$_i$ ratio and not on the absolute concentrations (Figure S6). Hence, we present our results in terms of the (Ag/NC)$_i$ ratio, which is a convenient description of the doping conditions, as will be shown below.

Inductively coupled plasma mass spectrometry (ICP-MS) measurements were conducted to correlate between the (Ag/NC)$_i$ ratio in solution and the actual number of Ag impurities per NC, denoted as (Ag/NC)$_a$. For these measurements, the doped NCs were isolated from the solution by solvent/antisolvent precipitation
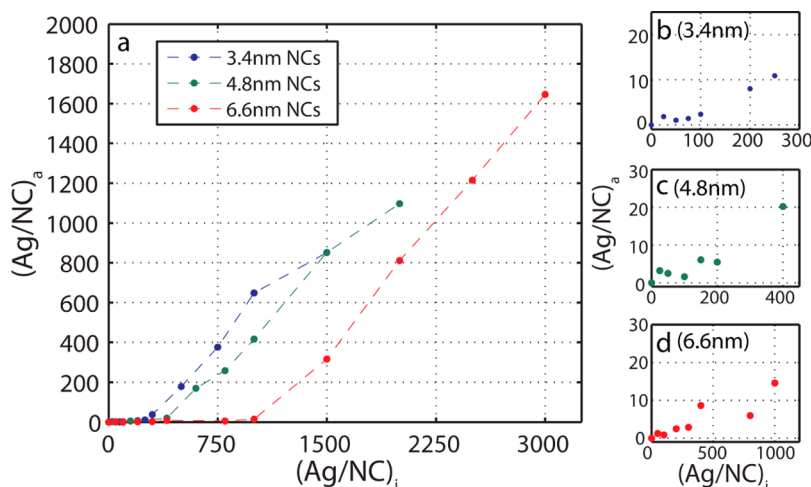
Figure 2. Measurement of the $(Ag/NC)_a$ ratio by ICP-MS measurements for 3.4 nm (blue), 4.8 nm (green), and 6.6 nm (red) InAs NCs as a function of the $(Ag/NC)_i$ ratio in solution. (a) Full range of Ag ratios for the three NC sizes; (b—d) zoom-ins showing the region of low ratios for the three NC sizes.

and were then dissolved in concentrated nitric acid (HNO_3 70%) and diluted with triply distilled water (for additional information see the Experimental Methods). ICP-MS results (Figure 2) for a series of 3.4 nm (blue), 4.8 nm (green), and 6.6 nm (red) InAs NC doped with various ratios of Ag atoms reveal two distinct regions. The first region, observed for the low $(Ag/NC)_i$ ratios, indicates that only few impurities are present in each NC (see Figure 2c,d and Figure S7 for zoom-in view on the doping region limits) and is therefore considered and termed herein as the "doping region", as further established below. The second region, reached when crossing a size-dependent threshold ratio of Ag atoms, is accompanied by a large increase in the $(Ag/NC)_a$ ratio, indicating a strong accumulation of Ag onto the NCs after this threshold, and is considered herein as the "growth regime".

The onset of the growth phase as a function of the $(Ag/NC)_i$ ratio was found to increase with NC size (Figure 2). One question that we can address with the help of the available data is the correlation between the observed crossover value between the two regions and the dimensionality of the NCs. By fitting each portion of the ICP-MS data with a linear function (Figure S7) we were able to extract the crossover values for each NC size and found that the transition from the "doping region" to the "growth region" occurs for $(Ag/NC)_i$ ratios of 222 ± 50, 395 ± 55, and 1130 ± 140 for the 3.4, 4.8, and 6.6 nm InAs NCs, respectively. Below these crossover points only a few Ag atoms are detected inside the NC (9, 12, or 14 (Figure S9), as detected by the ICP-MS, while the error bars on these numbers are correspondingly large.

To investigate the relationship between the crossover points (for different particle sizes) and the dimensionality of the NC, we plotted their values for each size of NC in terms of the linear, quadratic, or cubic functions of the NC radius. A cubic dependence on radius
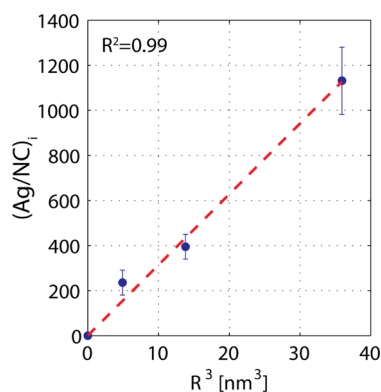
Figure 3. Linear fit of the $(Ag/NC)_i$ ratios in the solution, at the onset of the "growth region", as a function of the NC volume for the different NC sizes.

(*i.e.*, volume dependence) provided the best fit (Figure 3 and SI Figure S8). Hence, the measured values of the crossover points of the $(Ag/NC)_i$ ratios have a meaning of the solubility limit. Also, its determination through the $(Ag/NC)_i$ ratios in solution as opposed to the $(Ag/NC)_a$ ones determined by ICP-MS is better justified because the former are larger in value and better defined than the latter.

Plotting the electronic shift as a function of the $(Ag/NC)_a$ value (Figure 4) also reveals the two different regions within each size of NCs, similar to the aforementioned ICP-MS data. Here, the first region (*i.e.*, the "doping region"), taking place below the estimated "solubility limit", exhibits a substantial effect on the absorption spectrum of the NCs, whereas the second region (*i.e.*, the "growth region") has an overall negligible effect on the absorption. For the case of the 3.4 nm NCs (blue), the band gap energy has decreased by approximately 80 meV for a doping level of ~8 Ag atoms per NC (equivalent to a concentration of 200 Ag atoms per NC in solution), while it remains relatively unchanged for higher doping levels, decreasing only
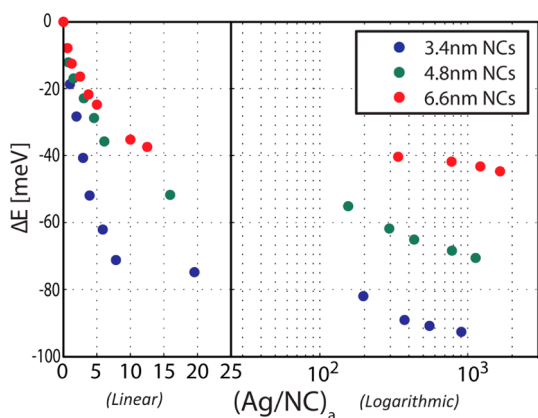
Figure 4. Energy shift of the first exciton peak as a function of $(Ag/NC)_a$ for the 3.4 nm (blue), 4.8 nm (green), and 6.6 nm (red) InAs NCs.

by an additional 10 meV for nearly 1000 Ag atoms per NC. This stands to show that the intersection point of these two regions coincides with the estimated solubility limit for each NC size, as extracted from the ICP-MS measurements.

XANES and EXAFS Data Analysis and Modeling. To further investigate the doping mechanism and the formation of two reaction regions indicated by the optical and ICP spectroscopy data and to elucidate the resulting structure in the doped semiconductor NCs, we employed X-ray absorption fine structure spectroscopy techniques. XAFS methods are sensitive to the local atomic environment and electronic properties of X-ray-absorbing atoms and their immediate surroundings, within *ca*. 0.5−0.8 nm radius from the absorber.[42] They therefore can shed light on the impurity diffusion mechanisms and interactions with the NC host. In our work, XAFS measurements were carried out by depositing the doped NC sample onto a Kapton tape and mounting the sample into a sealed sample chamber while in a nitrogen glovebox. The sample chamber was then transferred to the beamline, where it was connected to nitrogen flow to maintain inert conditions throughout (see Experimental Methods for more information).

First, in order to better understand the mechanism by which the doping occurs, we have performed solution-phase Ag K-edge XAFS measurements on the impurity solution, containing the metal salt and the appropriate ligands (see Experimental Methods for more details), and analyzed the experimental data (Figure S10). The best fit results for the impurity solution (see SI Table S1) revealed the presence of Ag−Br bonds but no Ag−N, Ag−O, or Ag−Ag bonds, indicating the complete dissociation of the $AgNO_3$ structure in the doping precursor solution and the formation of a ligand−impurity complex with no evidence of metal bonds. The presence of Ag−Br bonds in the doping solution and their absence in the doped samples (see below) sheds light on the mechanism of the doping.

As discussed previously, DDAB, which acts as a coordinating ligand, stabilizes the Ag(I) species in the organic medium. The Ag impurities adsorb from the solution to the surface of the NC, allowing then for its possible entry into the NC. To further elucidate the role of each constituent in the doping solution, three solutions of NCs, of similar size and concentration, were doped to the same $(Ag/NC)_i$ using either $AgNO_3$ in DDA, $AgNO_3$ in DDAB, or $AgNO_3$ in DDA+DDAB (Figure S11). The use of an impurity solution containing the metal salt and DDA resulted in an immediate loss of the first exciton feature with no clear optical absorption shift. Doping with an impurity solution containing only DDAB and the metal salt yields similar optical shifts to those achieved by doping using the impurity solution containing the metal salt and both DDA and DDAB. Therefore, we suggest a doping mechanism where the impurities are initially introduced into the NC as Ag(I), followed by the reduction of the Ag(I) to Ag(0), by the DDA, on the surface of the NC once the "solubility limit" is reached.

The X-ray absorption near edge structure (XANES) spectra, as collected from the In and As K-edges for all three NC sizes (Figure S12), reveal that the position of the absorption edge of both As and In edges does not change with $(Ag/NC)_i$ ratios, consistent with essentially unchanged charge states of both In and As.

However, for low $(Ag/NC)_i$ ratios, the XANES spectra of the Ag K-edge (Figure 5) as measured for 3.4, 4.8, and 6.6 nm InAs NCs appear to be nearly featureless above the absorption edge. This is indicative of a significant disordering of the environment around the Ag atoms. Due to the ensemble-averaging nature of XAFS, it is impossible, using a measurement of a single sample or a single state of a given sample, to determine whether the disorder is large around each Ag atom, all of which are crystallographically equivalent, or if there is a heterogeneity in Ag placements in the InAs lattice, which causes the large disorder in the average configuration of neighbors around Ag. As the $(Ag/NC)_i$ ratio increases, the fine structure above the absorption edge starts to be visible, and for the highest $(Ag/NC)_i$ ratio of all three NC sizes, the structure of the spectrum resembles that of the metallic Ag reference, indicative of the formation of a metallic state.

Figure 6 shows the Fourier-transform magnitudes of the extended X-ray absorption fine structure (EXAFS) spectra for the 3.4 nm (a), 4.8 nm (b), and 6.6 nm (c) Ag-doped NCs measured from the Ag K-edge. The *k*-range used for the above Fourier transform was 2−12 Å^{-1} for the In K-edge, 2−13 Å^{-1} for the As K-edge, and 2−11.4 Å^{-1} for the Ag K-edge (for representative *k*-space spectra of the EXAFS data of the 4.8 nm NCs see Figure S13). Visual examination of the EXAFS data indicates that for both As and In edges (Figure S14) the position of the main *R*-space peak is maintained and no new peaks evolve upon doping. This is consistent with
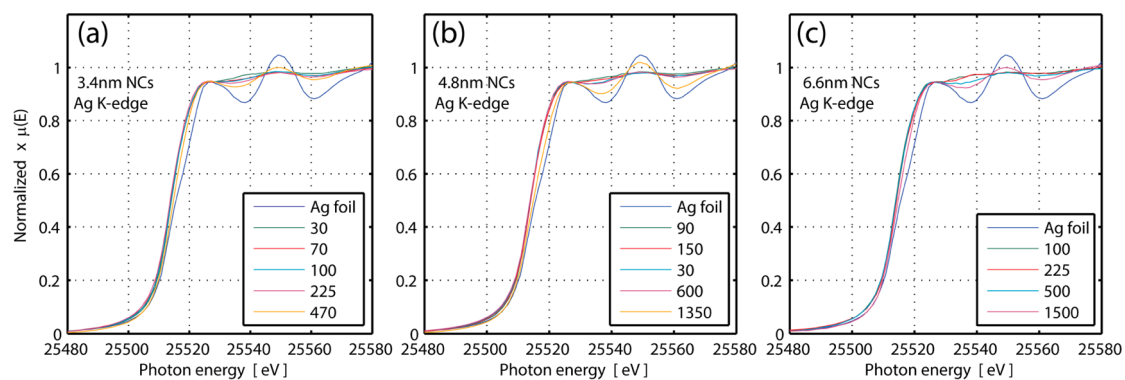
Figure 5. Ag K-edge XANES spectra for (a) 3.4 nm, (b) 4.8 nm, and (c) 6.6 nm InAs NCs doped with Ag. The legend depicts the $(Ag/NC)_i$ ratios in the solution.
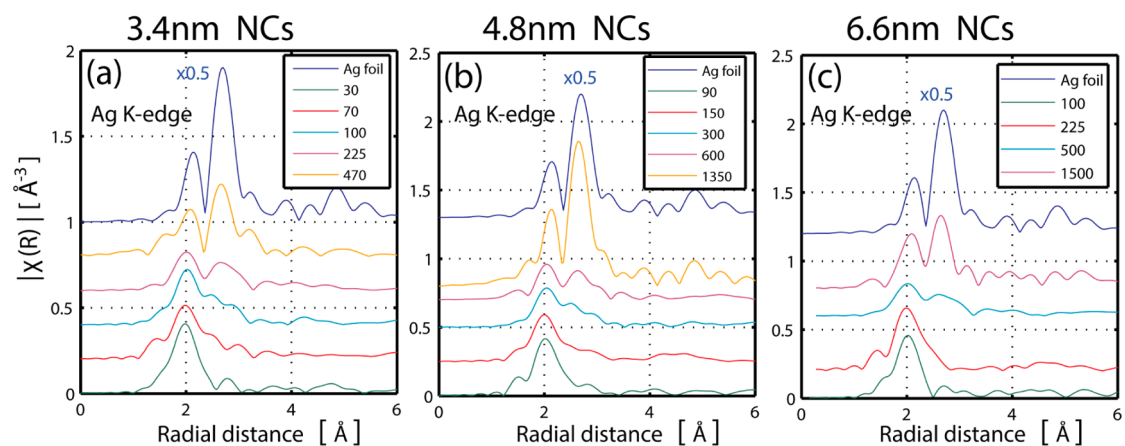

Figure 6. Fourier-transform magnitudes of the EXAFS spectra at different $(Ag/NC)_i$ ratios in solution for the Ag K-edge of the 3.4 nm (a), 4.8 nm (b), and 6.6 nm (c) Ag-doped InAs NCs. The spectra are offset vertically for clarity of presentation. The spectrum of the Ag reference foil is scaled down by a factor of 0.5. The legends depict the $(Ag/NC)_i$ ratios in solution.

substitutional doping, indicated also by the XANES spectra (Figure S12), where Ag substitutes for In in the InAs lattice. This is in contrast to the behavior observed by us previously for Cu-doped InAs NCs, which is an interstitial dopant, and, accordingly, its incorporation in interstitial sites is directly evidenced by the appearance of new peaks for the In and As in their EXAFS spectra and the formation of isosbestic points in both As and In XANES spectra.[38]

Unlike the In and As K-edges, the Ag K-edge data do change upon increasing the doping level. For low Ag levels, all the different sized NCs exhibit an apparent single R-space peak in the Ag EXAFS data, around $R \approx$ 2 Å (Figure 6a−c). This peak is distinctly different from the Ag−Ag spectra of pure Ag reference foil and can be explained by Ag−As contribution only, indicating that at low $(Ag/NC)_i$ ratios no metallic Ag is formed in either samples. Increasing the $(Ag/NC)_i$ ratio beyond the "solubility limit" results in the appearance of a second peak around $R \approx 3$ Å, in the region of Ag−Ag contribution of the bulk Ag. These changes, which will be confirmed by quantitative data analysis (*vide infra*), correspond to the formation of metallic Ag at higher Ag doping levels.

These observations for Ag are consistent with the following scenario: first, at low $(Ag/NC)_i$ ratios the preservation of EXAFS and XANES signals for the In and As edges is consistent with Ag doping, where Ag occupies substitutional (In) sites and is not at interstitial sites.[38] Indeed, p-type behavior was observed by us for Ag in InAs,[31] consistent with substitutional doping. Additional support for this model is gained from the Ag K-edge EXAFS data behavior (Figure 6a−c), dominated by the Ag−As contribution, as also evidenced by the quantitative data analysis. Thus, a structural model wherein Ag is a substitutional dopant was constructed and used to fit the data in this regime (Figure S15).

Further details and insight into the Ag doping behavior in these low $(Ag/NC)_i$ ratios is obtained from the quantitative results (Table S2 and Figure S16). The best fit results consist of (i) the coordination numbers (N) for the different neighbors surrounding the Ag atom, (ii) the interatomic distances (R) between the Ag and its nearest neighbors, (iii) the mean square deviations of the interatomic bond lengths, also known as EXAFS Debye−Waller factors (σ^2) for each bond, and (iv) the changes in the photoelectron energy origin (ΔE_0).

As seen in SI Table S2, the best fit results for the Ag—As coordination number (at low (Ag/NC)$_i$ ratios) yield an average coordination number closer to $N = 2$, rather than to $N = 4$ (Table S2). Attempting to constrain the Ag—As coordination number to be exactly $N = 4$ (for the lower (Ag/NC)$_i$ ratios) resulted in ΔE_0 values of -15 eV for the Ag K-edge, which are nonphysical. On the other hand, other contributions to Ag could be expected, such as Ag—N, due to the presence of amine-capping ligands. When added, the Ag—N contributions improved the fit, reducing both values of reduced chi-square and R-factor (Table S3). Together, these two parameters (Ag—As and Ag—N coordination numbers) and the fact that Ag—N bonds were not detected in the solution suggest that the Ag is situated predominantly on sites at the surface of the NCs. This model is different from that where Ag atoms are purely substitutional, i.e., spread in the NC uniformly. In the latter model, the coordination numbers of Ag—As would be the same as In—As, which are equal to 3.5, 3.7, and 3.7 for particles of 3.4, 4.8, and 6.6 nm, respectively. These numbers are in all cases larger than those obtained experimentally for Ag (Table S2).

However, sole surface binding of Ag atoms is inconsistent with the observed optical spectral red-shift. We have previously modeled the contribution of surface strain to the evolution of the electronic properties of the InAs NCs upon doping and found that purely surface-bound impurities could not induce electronic shifts on the order of 100 meV.[31] This notion, together with the featureless XANES spectrum (Figure 5) and the averaged coordination numbers (Table S2) for the low (Ag/NC)$_i$ ratios, suggests a more intricate explanation. The emerging behavior is one in which the Ag has, in fact, a diverse heterogeneous surrounding, where some of the impurities are substitutional dopants and the rest are surface bound, occupying in particular As dangling bonds. This inhomogeneous distribution can result in such average behavior since the EXAFS method indeed provides the ensemble average data for the sample. This more elaborate view for Ag doping in InAs NCs is also in line with the intricate structure of Ag doping in CdSe studied by Norris and co-workers, which demonstrated the repulsion of Ag impurities to the surface of the NC, where they assumed both interstitial and substitutional lattice sites.[32,39] However, unlike the system described by Norris et al., attempts to allow for both Ag—As and Ag—In bonds (as would result from Ag being an interstitial impurity[38]) resulted in unphysically large ΔE_0 for the Ag—In bond, indicating this type of binding is not favored by the fit.

Another interesting parameter obtained by the fit (Table S2) is the interatomic (R) distance between the probed atom and its surrounding neighbors. Figure 7 depicts the Ag—As (green) and In—As (black) interatomic distance as a function of the (Ag/NC)$_a$ ratio for the 4.8 nm doped InAs NCs (for the 3.4 and 6.6 nm sized
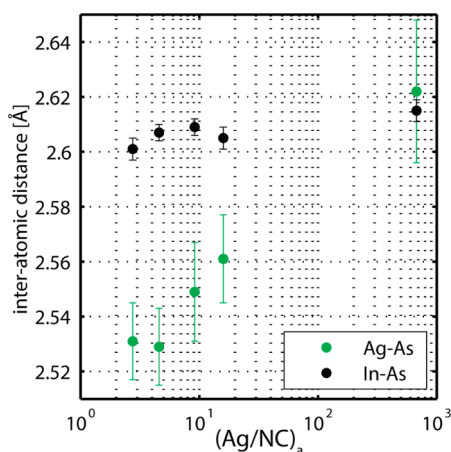
Figure 7. Ag—As (green) and In—As (black) interatom distances extracted from the EXAFS fitting results, as a function of the (Ag/NC)$_a$ values for the 4.8 nm doped InAs NCs.

NCs, see SI Figure S17). As can be seen, the In—As bond length is unaffected by the doping for all three NC sizes, suggesting that the lattice structure is generally preserved during the doping process considering the large numbers of these original NC atoms (as can also be deduced from the small Debye—Waller factor; see SI Table S2). The Ag—As bond length, however, was found to expand in all three NC sizes when increasing the (Ag/NC)$_a$ ratio.

As already discussed above, the solubility limit is on the order of a few to tens of Ag atoms per NC. Interestingly, as Figure 7 demonstrates, for Ag doping levels under the solubility limit, the Ag—As bond length is shorter than that of In—As. The issue of impurity—host bond lengths in semiconductors has been discussed previously for isovalent impurities, suggesting that the host—impurity bond length is strongly affected by the size of the substituting atom and the redistribution of charge density around the impurity—host bond.[43] Such changes in the impurity—host bond lengths were used in the case of doped ZnSe alloys to determine that the covalent radius of Co is slightly smaller than that of the Zn host atom within the crystal lattice.[44] More recently, a bimodal behavior was presented for Co-doped CdSe and ZnSe NCs owing to the differences in the ionic radii of the constituents.[45] However, the differences in the ionic radii of the host and the impurity alone are insufficient to rationalize our experimental results (Figure 7), which show a decrease in the Ag—As bond length at the impurity level (contradictory to the simple consideration where a larger impurity (Ag) should lead to a larger bond length when substituting for a smaller size host (In)). The explanation is in the change of effective ionic radius of As when Ag comes into its nearest neighbor position, compared to the undoped case. Such effect is possible due to the redistribution of the charge density around the Ag—As bond occurring upon doping in the InAs system, shifting the charge density from As—Ag

toward As—In bonds. Due to the low level of Ag impurities, the effect on the In—As bonds is minimal, and therefore no change is seen in the EXAFS results (Figure 7). Furthermore, this interpretation also agrees with the electronic model of Ag doping, in which the Ag(I) acts as an acceptor in the InAs lattice, yielding a p-type NC.

We next discuss the second, growth regime, beyond the solubility limit of the Ag impurities. As interpreted in the visual examination of the EXAFS data (Figure 6), an increase in the (Ag/NC)$_i$ ratio results in the formation of metallic characteristics, represented by the Ag—Ag interaction in the fit results (Table S2). The (Ag/NC)$_i$ ratios at which Ag—Ag bonds start to appear increase with the size of the NCs, consistent with the previously discussed optical absorption and ICP-MS measurements. However, whereas all previous measurements (ICP-MS, optical absorption, and XANES analysis) indicate the strong accumulation of Ag occurs only beyond a (Ag/NC)$_i$ ratios of 200, 400, and 1000, for the 3.4, 4.8, and 6.6 nm NCs, respectively, the EXAFS best fit results indicate that some Ag—Ag bonds are present already at (Ag/NC)$_i$ ratios of 100, 300, and 500 Ag atoms for the respective sizes. This suggests that while Ag—Ag interactions start forming rather early, at low (Ag/NC)$_i$ ratios, the Ag clusters are not nucleated and formed until the solubility limit is reached, after which these metallic phases act as nucleation sites for rapid Ag accumulation.

The EXAFS best fit results (Table S2) show that the highest doping levels for the 3.4, 4.8, and 6.6 nm samples yield average Ag—Ag coordination numbers of 4.2 ± 0.6, 7.4 ± 0.6, and 5.0 ± 0.8, respectively. However, considering the (Ag/NC)$_a$ values for these samples (175−1000 atoms), we have calculated the average coordination number and found it should be in the range of 7−10 (for a detailed explanation see SI Figure S18). There could be two different reasons for this discrepancy. The first is the formation of numerous ultrasmall metal clusters (that lower the average metal—metal coordination number) on the surface of the NCs, and the second is the manner by which EXAFS obtains the coordination numbers in the case when two or more environments of Ag atoms are mixed together in the sample, e.g., substitutional Ag—As, surface-bound Ag—As, and Ag—Ag.[46] We note in this regard that the interatomic distance of the Ag—Ag bonds, as indicated by Table S2, shows almost no change when increasing the Ag content in the solution phase. This differs from the expected trend for the growth of spherical-like metallic clusters, which are reported to have an initially reduced interatomic bond length compared to their bulk counterpart (2.87 Å) and expand as the particle grows in size,[47,48] further supporting the idea of the Ag having a heterogeneous surrounding and a non-homogeneous metal growth on the surface of the NC.
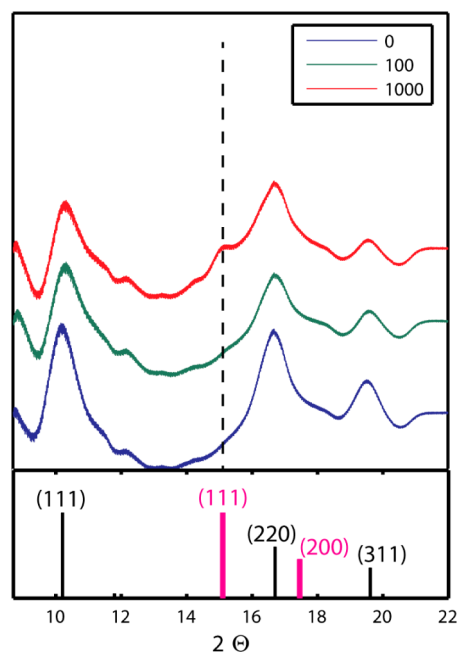
Figure 8. Synchrotron-based powder XRD measurements (λ = 0.62 Å) for 4.8 nm InAs NCs doped to various (Ag/NC)$_i$ ratios. Bottom panes represent the standard diffraction peaks for InAs zincblende lattice (black bars) and metallic Ag FCC (magenta bars). The dashed line represents the position of the (111) Ag crystal plane.

This was further corroborated by powder XRD measurements that were performed on Ag-doped InAs samples. XRD data of 4.8 nm InAs NCs doped with different (Ag/NC)$_i$ ratios (Figure 8) indicate that for low (Ag/NC)$_i$ ratios the main InAs reflections are preserved and no new peaks appear in the spectrum (see Figure S19 for XRD spectra of 3.4 and 6.6 nm doped NCs). However, a new diffraction peak appears at $2\theta =$ 15 deg (indicated by the arrow), identified as the (111) Ag crystal plane, upon reaching high doping ratios. This indicates that while Ag—Ag interactions may be present already at low (Ag/NC)$_i$ ratios (as indicated by the EXAFS results), they are characterized by low crystallinity, and it is only past the "solubility limit" that metallic structures are formed on the surface of the NC, in agreement with all the previously interpreted data.

Conclusions. A study of diffusion-based Ag doping in presynthesized InAs NCs of different sizes was carried out. Optical absorption and ICP-MS measurements indicated two different regions that depend on the (Ag/NC)$_i$ ratio in the solution: the "doping region" at low (Ag/NC)$_i$ ratios and the "growth region" at high ratios. A combination of advanced XAS and XRD measurements resulted in a structural model of Ag(I) initially substituting for In atoms near the surface of the NC followed by the formation of Ag metallic structures on the NC surface. As the (Ag/NC)$_i$ ratio increases, larger metallic clusters begin to form, acting as nucleation sites and preventing additional doping of the NC, which has already reached the Ag solubility limit.

The results presented here provide insight toward the "doping limit" of colloidal semiconductor NCs, which has not been observed in previous diffusion-based doping reactions such as Cu doping in InAs,[38] Ag doping in CdSe,[32] or Mn doping in CdSe.[33] This kind of understanding of various behaviors of semiconductor nanocrystal doping scenarios is a necessary prerequisite for the rational design of doped nanocrystals with desired properties. Availability of such doped nanocrystals may open a path for further development of advanced optoelectronic devices based on heavily doped semiconductor NCs.

EXPERIMENTAL METHODS

Colloidal InAs NCs. These were synthesized following a well-established wet-chemical synthesis.[40] Precursor solutions containing (TMS)$_3$As (tris(trimethylsilyl)arsine) and InCl$_3$ (indium(III) chloride) were prepared in a nitrogen glovebox (MBraun) and kept under inert conditions throughout the reaction. A solution of distilled trioctylphosphine was evacuated for ~30 min and then heated to 300 °C. The nucleation solution was rapidly injected, and the solution temperature lowered to 260 °C. The growth solution was then gradually introduced to the solution, allowing particle growth until the desired size is reached. Narrow size distributions were further achieved through size-selective precipitation performed in a glovebox by adding methanol to the NC dispersion and filtering the solution through a 0.2 um polyamide membrane filter (Whatman).

Doping of Presynthesized InAs NCs. This was achieved *via* a room-temperature solution-phase reaction previously reported by us.[31] Briefly, an impurity Ag stock solution was prepared by dissolving 10 mg (0.058 mmol) of the metal salt (AgNO$_3$), 80 mg (0.17 mmol) of DDAB, and 120 mg (0.64 mmol) of DDA in 10 mL of anhydrous toluene (Sigma). Calculated amounts (v/v) of the impurity solution were added to a suspension of InAs NCs, according to the desired (Ag/NC)$_i$ ratio, while stirring. The concentration of the NCs was estimated based on the literature values of the InAs NC absorption cross-section.[49] The doping reaction was performed under inert conditions in a glovebox, and the reaction was terminated after 15 min by adding methanol and isolating the doped NCs through precipitation.

ICP-MS Measurements. Inductively coupled plasma mass spectroscopy was carried out in an Agilent 7500cx in order to correlate between the solution ratio and the actual number of impurities per NC. First, the NC samples were dried under vacuum, after which they were dissolved in a 70% HNO$_3$ solution (Sigma) and diluted to a final concentration of 3% HNO$_3$ with triply distilled water. The impurity concentration was calculated *versus* a calibration curve based on reference samples prepared using a 1000 ppm standard solution (High Purity Standards). Prior to the analysis, the ICP-MS was calibrated with a series of multielement standard solutions (1 ng/l to 100 mg/L Merck ME VI) and standards of major metals (300−3 mg/L). Internal standard (50 ng/mL Sc, 5 ng/mL Re and Rh) was added to every standard and sample for drift correction.

XAFS Measurements. These were performed at the Brookhaven National Laboratory National Synchrotron Light Source beamline X18B. The specimens were prepared under inert conditions in a glovebox (MBraun), where they were spread on adhesive tape and mounted in a sample chamber. The chamber, filled with nitrogen, was then transferred to the beamline, where it was flushed with nitrogen during the measurements to maintain inert conditions through the experiments. Experiments at the As and In K-edges were performed in transmission mode, and for the Ag K-edge, both in transmission and fluorescence. Three to 10 consecutive measurements were taken at each edge to improve the signal-to-noise ratio in the data.

XAFS Data Analysis and Processing. This was done using standard techniques. Briefly, the data were first aligned in energy, using reference spectra collected in standard materials together simultaneously with the NC data, and then averaged. Next, the smooth, isolated atom background function was subtracted from the absorption coefficient using the Athena program[50] from the IFEFFIT package.[51]

In all fits, theoretical photoelectron scattering amplitudes and phases were calculated using the program FEFF6.[52] With the purpose of improving the reliability of the fit, for each sample size and each absorption edge, the fitting process was performed simultaneously for the different doping levels. For Ag K-edge EXAFS fits, Ag−As, Ag−N, and/or Ag−Ag paths were included in the fitting model. The reduction factor ($S_0{}^2 = 0.95$) was found from the fit to the bulk Ag and fixed in the fits to the doped NC data. Adjustable parameters in the theoretical EXAFS signal included the coordination numbers of nearest neighbors of a certain type around the absorbing Ag atom (N), the bond distance between the absorber and the nearest neighbors (R), and its mean-square-displacement (σ^2). While these three variables (N, R, and σ^2) change with the doping levels, the corrections to the photoelectron energy origins (ΔE_0) were varied independently for each neighboring pair but constrained to be the same for all doping concentrations of a certain sized sample. For In and As K-edge EXAFS fits, only one path was used for fitting. It is In−As for In edge data and As−In/Ag for As edge (the photoelectron scattering features of In and Ag are similar and cannot be discriminated in XAFS fitting), and their coordination number was constrained to be 4. Similar to the strategy used for fitting Ag edge data, R and σ^2 were global variables, while ΔE_0 was constrained to be the same for all doping levels of each sized sample. The reduction factors ($S_0{}^2 = 0.89$ for both In and As) for In and As edge data were obtained by fitting InAs QDs. The fitting range in k space is 2−11.4 Å^{-1} for Ag, 2−12 Å^{-1} for In, and 2−13 Å^{-1} for As. The fitting range in R space is 1.4−3.0 Å for Ag, 1.8−2.9 Å for In, and 1.8−2.8 Å for As. For Ag edge spectra, the fitting k weight is 2, while it is 3 for fitting both In and As edge spectra.

XRD Measurements. These were performed at the Brookhaven National Laboratory National Synchrotron Light Source beamline X18A. The specimens were prepared under inert conditions in a glovebox (MBraun), where they were spread on adhesive tape. XRD patterns were acquired with a PerkinElmer (PE) amorphous silicon detector with 2048 × 2048 pixels and a 200 × 200 μm^2 pixel size. The detector is mounted on the 2θ arm; the typical 2θ range is 5° to 22°. The energy of the beam was set to 20 keV. Before spectra collection, the detector was calibrated using a LaB$_6$ standard. For each spectrum, multiple scans were recorded for both the diffraction pattern and the dark current, which was subtracted.

Conflict of Interest: The authors declare no competing financial interest.

Supporting Information Available: The Supporting Information is available free of charge on the ACS Publications website at DOI: 10.1021/acsnano.5b03044.

UV−vis absorption spectra and ICP-MS measurements for additional NC sizes doped with various impurity concentrations. XAS As K-edge and In K-edge spectra for additional NC sizes as well as impurity solution measurements. Structural model used for fitting EXAFS data, best fit results for all NC sizes and (Ag/NC)$_i$ ratios, and theoretical calculations of ideal metallic clusters' coordination numbers (PDF)

REFERENCES AND NOTES

1. Alivisatos, A. P. Perspectives on the Physical Chemistry of Semiconductor Nanocrystals. *J. Phys. Chem.* **1996**, *100*, 13226–13239.

2. Brus, L. E. A Simple Model for the Ionization Potential, Electron Affinity, and Aqueous Redox Potentials of Small Semiconductor Crystallites. *J. Chem. Phys.* **1983**, *79*, 5566–5571.

3. Murray, C. B.; Norris, D. J.; Bawendi, M. G. Synthesis and Characterization of Nearly Monodisperse CdE (E = Sulfur, Selenium, Tellurium) Semiconductor Nanocrystallites. *J. Am. Chem. Soc.* **1993**, *115*, 8706–8715.

4. Guzelian, A. A.; Banin, U.; Kadavanich, A. V.; Peng, X.; Alivisatos, A. P. Colloidal Chemical Synthesis and Characterization of InAs Nanocrystal Quantum Dots. *Appl. Phys. Lett.* **1996**, *69*, 1432–1434.

5. Murray, C. B.; Sun, S.; Gaschler, W.; Doyle, H.; Betley, T. A.; Kagan, C. R. Colloidal Synthesis of Nanocrystals and Nanocrystal Superlattices. *IBM J. Res. Dev.* **2001**, *45*, 47–56.

6. Peng, X.; Manna, L.; Yang, W.; Wickham, J.; Scher, E.; Kadavanich, A.; Alivisatos, A. P. Shape control of CdSe nanocrystals. *Nature* **2000**, *404*, 59–61.

7. Lu, W.; Fang, J.; Ding, Y.; Wang, Z. L. Formation of PbSe Nanocrystals: A Growth Toward Nanocubes. *J. Phys. Chem. B* **2005**, *109*, 19219–19222.

8. Warner, J. H.; Cao, H. Shape Control of PbS Nanocrystals Using Multiple Surfactants. *Nanotechnology* **2008**, *19*, 305605−1−305605−5.

9. Talapin, D. V.; Nelson, J. H.; Shevchenko, E. V.; Aloni, S.; Sadtler, B.; Alivisatos, A. P. Seeded Growth of Highly Luminescent CdSe/CdS Nanoheterostructures with Rod and Tetrapod Morphologies. *Nano Lett.* **2007**, *7*, 2951–2959.

10. Macdonald, J. E.; Bar Sadan, M.; Houben, L.; Popov, I.; Banin, U. Hybrid Nanoscale Inorganic Cages. *Nat. Mater.* **2010**, *9*, 810–815.

11. Rivest, J. B.; Swisher, S. L.; Fong, L.-K.; Zheng, H.; Alivisatos, A. P. Assembled Monolayer Nanorod Heterojunctions. *ACS Nano* **2011**, *5*, 3811–3816.

12. Gur, I.; Fromer, N. A.; Geier, M. L.; Alivisatos, A. P. Air-Stable All-Inorganic Nanocrystal Solar Cells Processed from Solution. *Science* **2005**, *310*, 462–465.

13. Talapin, D. V.; Murray, C. B. PbSe Nanocrystal Solids for n- and p-Channel Thin Film Field-Effect Transistors. *Science* **2005**, *310*, 86–89.

14. Kim, D. K.; Lai, Y.; Diroll, B. T.; Murray, C. B.; Kagan, C. R. Flexible and Low-Voltage Integrated Circuits Constructed From High-Performance Nanocrystal Transistors. *Nat. Commun.* **2012**, *3*, 1216–1222.

15. Sze, S. M.; Ng, K. K. In *Physics of Semiconductor Devices*; Wiley: Hoboken, NJ, 2006.

16. Willardson, R. K.; Beer, A. C. In *Physics of III-V Compounds*; Willardson, R. K., Beer, A. C., Eds.; Semiconductors and Semimetals 4; Academic Press: New York, 1968.

17. Dalven, R. A Review of the Semiconductor Properties of PbTe, PbSe, PbS and PbO. *Infrared Phys.* **1969**, *9*, 141–184.

18. Erwin, S. C.; Zu, L.; Haftel, M. I.; Efros, A. L.; Kennedy, T. A.; Norris, D. J. Doping Semiconductor Nanocrystals. *Nature* **2005**, *436*, 91–94.

19. Norris, D. J.; Efros, A. L.; Erwin, S. C. Doped Nanocrystals. *Science* **2008**, *319*, 1776–1779.

20. Buonsanti, R.; Milliron, J. D. Chemistry of Doped Colloidal Nanocrystals. *Chem. Mater.* **2013**, *25*, 1305–1317.

21. Yang, P.; Song, C.; Lü, M.; Zhou, G.; Yang, Z.; Xu, D.; Yuan, D. Photoluminescence of Cu+-Doped and Cu2+-Doped ZnS Nanocrystallites. *J. Phys. Chem. Solids* **2002**, *63*, 639–643.

22. Xie, R.; Peng, X. Synthesis of Cu-Doped InP Nanocrystals (ddots)with ZnSe Diffusion Barrier as Efficient and Color-Tunable NIR Emitters. *J. Am. Chem. Soc.* **2009**, *131*, 10645–10651.

23. Geyer, S. M.; Allen, P. M.; Chang, L.-Y.; Wong, C. R.; Osedach, T. P.; Zhao, N.; Bulovic, V.; Bawendi, M. G. Control of the Carrier Type in InAs Nanocrystal Films by Predeposition Incorporation of Cd. *ACS Nano* **2010**, *4*, 7373–7378.

24. Stavrinadis, A.; Rath, A.; de Arquer, F.; Diedenhofen, S. L.; Magén, C.; Martinez, L.; So, D.; Konstantatos, G. Heterovalent Cation Substitutional Doping for Quantum Dot Homojunction Solar Cells. *Nat. Commun.* **2013**, *4*, 2981–2988.

25. Bhargava, R. N.; Goorskey, D.; Hong, X.; Nurmikko, A. Optical Properties of Manganese-Doped Nanocrystals of ZnS. *Phys. Rev. Lett.* **1994**, *72*, 416–419.

26. Stowell, C. A.; Wiacek, R. J.; Saunders, A. E.; Korgel, B. A. Synthesis and Characterization of Dilute Magnetic Semiconductor Manganese-Doped Indium Arsenide Nanocrystals. *Nano Lett.* **2003**, *3*, 1441–1447.

27. Shim, M.; Guyot-Sionnest, P. N-Type Colloidal Semiconductor Nanocrystals. *Nature* **2000**, *407*, 981–983.

28. Rinehart, J. D.; Schimpf, A. M.; Weaver, A. L.; Cohn, A. W.; Gamelin, D. R. Photochemical Electronic Doping of Colloidal CdSe Nanocrystals. *J. Am. Chem. Soc.* **2013**, *135*, 18782–18785.

29. Bekenstein, Y.; Vinokurov, K.; Keren-Zur, S.; Hadar, I.; Schilt, Y.; Raviv, U.; Millo, O.; Banin, U. Thermal Doping by Vacancy Formation in Copper Sulfide Nanocrystal Arrays. *Nano Lett.* **2014**, *14*, 1349–1353.

30. Choi, J.-H.; Fafarman, A. T.; Oh, S. J.; Ko, D.-K.; Kim, D. K.; Diroll, B. T.; Muramoto, S.; Gillen, J. G.; Murray, C. B.; Kagan, C. R. Bandlike Transport in Strongly Coupled and Doped Quantum Dot Solids: A Route to High-Performance Thin-Film Electronics. *Nano Lett.* **2012**, *12*, 2631–2638.

31. Mocatta, D.; Cohen, G.; Schattner, J.; Millo, O.; Rabani, E.; Banin, U. Heavily Doped Semiconductor Nanocrystal Quantum Dots. *Science* **2011**, *332*, 77–81.

32. Sahu, A.; Kang, M. S.; Kompch, A.; Notthoff, C.; Wills, A. W.; Deng, D.; Winterer, M.; Frisbie, C. D.; Norris, D. J. Electronic Impurity Doping in CdSe Nanocrystals. *Nano Lett.* **2012**, *12*, 2587–2594.

33. Vlaskin, V. A.; Barrows, C. J.; Erickson, C. S.; Gamelin, D. R. Nanocrystal Diffusion Doping. *J. Am. Chem. Soc.* **2013**, *135*, 14380–14389.

34. Turnbull, D. Formation of Crystal Nuclei in Liquid Metals. *J. Appl. Phys.* **1950**, *21*, 1022–1028.

35. Edmond, J. T.; Hilsum, C. Heat Treatment Effects in Indium Arsenide. *J. Appl. Phys.* **1960**, *31*, 1300–1301.

36. Dalpian, G. M.; Chelikowsky, J. R. Self-Purification in Semiconductor Nanocrystals. *Phys. Rev. Lett.* **2006**, *96*, 226802-1–226802-4.

37. Chan, T.-L.; Tiago, M. L.; Kaxiras, E.; Chelikowsky, J. R. Size Limits on Doping Phosphorus into Silicon Nanocrystals. *Nano Lett.* **2008**, *8*, 596–600.

38. Amit, Y.; Eshet, H.; Faust, A.; Patllola, A.; Rabani, E.; Banin, U.; Frenkel, A. I. Unraveling the Impurity Location and Binding Energy in Heavily Doped Semiconductor Nanocrystals: The Case of Cu in InAs Nanocrystals. *J. Phys. Chem. C* **2013**, *117*, 13688–13696.

39. Ott, F. D.; Spiegel, L. L.; Norris, D. J.; Erwin, C. S. Microscopic Theory of Cation Exchange in CdSe Nanocrystals. *Phys. Rev. Lett.* **2014**, *113*, 156803–156808.

40. Cao; Banin, U. Growth and Properties of Semiconductor Core/Shell Nanocrystals with InAs Cores. *J. Am. Chem. Soc.* **2000**, *122*, 9692–9702.

41. Tauc, J. In *Amorphous and Liquid Semiconductors*; Plenum: New York, 1974.

42. Stern, E. A. Theory of EXAFS. In *X-ray Absorption: Principles, Applications, Techniques of EXAFS, SEXAFS, and XANES*; Koningsberger, D. C.; Prins, R., Eds.; Wiley: New York, 1988.

43. Martins, J. L.; Zunger, A. Bond Lengths Around Isovalent Impurities and in Semiconductor Solid Solutions. *Phys. Rev. B: Condens. Matter Mater. Phys.* **1984**, *30*, 6217–6220.

44. Lawniczak, K.-J.; Golacki, Z. Extended X-ray Absorption Fine Structure Studies of Co-Doped ZnS and ZnSe Alloys. *Acta Phys. Polym., A* **1994**, *86*, 727–735.

45. Santangelo, S. A.; Hinds, E. A.; Vlaskin, V. A.; Archer, P. I.; Gamelin, D. R. Bimodal Bond-Length Distributions in Cobalt-Doped CdSe, ZnSe, and $Cd_{1-x}Zn_xSe$ Quantum Dots. *J. Am. Chem. Soc.* **2007**, *129*, 3973–3978.

46. Frenkel, A. I. Solving the 3D structure of metal nanoparticles. *Z. Kristallogr.* **2007**, *222*, 605–611.

47. Frenkel, A. I.; Hills, C. W.; Nuzzo, R. G. A View from the Inside: Complexity in the Atomic Scale Ordering of Supported Metal Nanoparticles. *J. Phys. Chem. B* **2001**, *105*, 12689–12703.

48. Frenkel, A. I.; Nemzer, S.; Pister, I.; Soussan, L.; Harris, T.; Sun, Y.; Rafailovich, M. H. Size-Controlled Synthesis and Characterization of Thiol-Stabilized Gold Nanoparticles. *J. Chem. Phys.* **2005**, *123*, 184701-1–184701−6.

49. Yu, P.; Beard, M. C.; Ellingson, R. J.; Ferrere, S.; Curtis, C.; Drexler, J.; Luiszer, F.; Nozik, A. J. Absorption Cross-Section and Related Optical Properties of Colloidal InAs Quantum Dots. *J. Phys. Chem. B* **2005**, *109*, 7084–7087.

50. Ravel, B.; Newville, M. ATHENA, ARTEMIS, HEPHAESTUS: Data Analysis for X-Ray Absorption Spectroscopy Using IFEFFIT. *J. Synchrotron Radiat.* **2005**, *12*, 537–541.

51. Newville, M. IFEFFIT: Interactive XAFS Analysis and FEFF Fitting. *J. Synchrotron Radiat.* **2001**, *8*, 322–324.

52. Zabinsky, S. I.; Rehr, J. J.; Ankudinov, A.; Albers, R. C.; Eller, M. J. Multiple-Scattering Calculations of X-Ray-Absorption Spectra. *Phys. Rev. B: Condens. Matter Mater. Phys.* **1995**, *52*, 2995–3009.